RESEARCH ARTICLE

Droplet-based bioprinting enables the fabrication of cell–hydrogel–microfibre composite tissue precursors

Marcin Kotlarz[1] · Ana M. Ferreira[1] · Piergiorgio Gentile[1] · Stephen J. Russell[2] · Kenneth Dalgarno[1]

Abstract

Composites offer the option of coupling the individual benefits of their constituents to achieve unique material properties, which can be of extra value in many tissue engineering applications. Strategies combining hydrogels with fibre-based scaffolds can create tissue constructs with enhanced biological and structural functionality. However, developing efficient and scalable approaches to manufacture such composites is challenging. Here, we use a droplet-based bioprinting system called reactive jet impingement (ReJI) to integrate a cell-laden hydrogel with a microfibrous mesh. This system uses microvalves connected to different bioink reservoirs and directed to continuously jet bioink droplets at one another in mid-air, where the droplets react and form a hydrogel that lands on a microfibrous mesh. Cell–hydrogel–fibre composites are produced by embedding human dermal fibroblasts at two different concentrations (5×10^6 and 30×10^6 cells/mL) in a collagen–alginate–fibrin hydrogel matrix and bioprinted onto a fibre-based substrate. Our results show that both types of cell–hydrogel–microfibre composite maintain high cell viability and promote cell–cell and cell–biomaterial interactions. The lower fibroblast density triggers cell proliferation, whereas the higher fibroblast density facilitates faster cellular organisation and infiltration into the microfibres. Additionally, the fibrous component of the composite is characterised by high swelling properties and the quick release of calcium ions. The data indicate that the created composite constructs offer an efficient way to create highly functional tissue precursors for laminar tissue engineering, particularly for wound healing and skin tissue engineering applications.

Graphic abstract
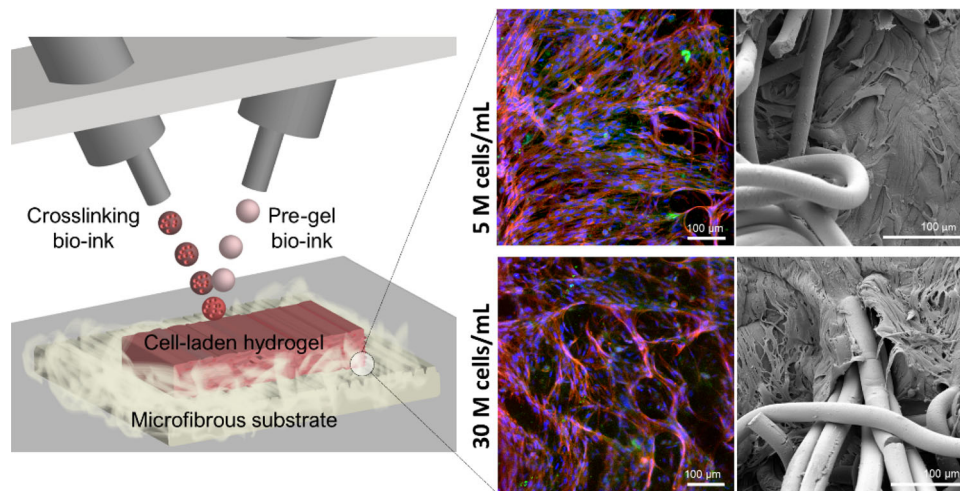
✉ Kenneth Dalgarno
kenny.dalgarno@ncl.ac.uk

1 School of Engineering, Newcastle University, Newcastle upon Tyne NE1 7RU, UK

2 School of Design, University of Leeds, Leeds LS2 9JT, UK

Introduction

Bioprinting, a technology converging tissue engineering and additive manufacturing, has emerged in recent years as an attractive strategy for co-processing cells and biomaterials for the fabrication of three-dimensional (3D) cell-laden scaffolds [1]. Such constructs provide greater spatial depth and better cell–cell communication for the enhanced biomimicking of physiological conditions [2]. The development of bioprinting has brought novel research directions to various areas of regenerative medicine, e.g. cartilage [3, 4], bone [5, 6], wound healing and skin regeneration [7, 8].

A wide range of synthetic and natural biomaterials serving as bioinks are compatible with different bioprinting techniques. Regardless of their origin, these materials must meet certain criteria for successful cell incorporation. Hydrogels are hydrophilic polymer networks that show low cytotoxicity and similarities with the native extracellular matrix (ECM) [9]. The aqueous network structure of hydrogels provides a favourable environment for cell encapsulation, making them attractive materials for bioprinting applications [10, 11]. However, hydrogels facilitating extensive cell differentiation and proliferation are naturally soft and thus are challenged by their weak mechanical properties [12]. Soft and aqueous hydrogel structures are difficult to handle in a clinical set-up. Therefore, combining hydrogels with other structural biomaterials could create more biologically functional and reinforced tissue-engineered constructs.

To this end, strategies to fabricate composites by integrating hydrogels and fibre-based scaffolds have been of particular interest [13, 14]. Hydrogel–fibre composites can potentially improve problems that arise throughout the lifecycle of the scaffolds, such as handling and mechanical strength issues of the hydrogel matrices, or poor cellular adhesion and infiltration to the fibre-based scaffolds. However, current strategies to fabricate hydrogel–fibre composites are limited in terms of achievable cell incorporation and cell seeding density. Seeding the cells after composite fabrication is potentially the most straightforward approach but results in hindered cell infiltration and spatial communication between cells [15]. The integration of hydrogels and fibrous meshes has been achieved by means of hydrogel electrospraying [16], co-electrospinning [17], co-extrusion of matrix/fibre scaffolds followed by cross-linking [18], simple in situ cross-linking [19] and hydrogel covalent linking to fragmented electrospun fibres [20]. Extrusion-based bioprinting with melt electrowriting was also demonstrated as a feasible way to produce a cell–hydrogel–fibre scaffold [21]. However, several challenges remain for hydrogel–cell–fibre composites, including: (i) Achieving a homogeneous distribution of cells, particularly at high cell densities; (ii) Control over the architectural organisation of the matrix; (iii) Low productivity.

From the perspective of fibre structure, one highly productive technique that has not been extensively researched for tissue engineering applications is the fabrication of non-woven needle-punched fabrics. In this technique, a wide range of raw materials in the form of staple fibres or continuous filaments can be assembled into a web, which is then bonded by oscillating barbed metal needles through the fibrous assembly to generate fibre entanglement, frictional resistance and therefore mechanical bonding [22]. Nonwoven needle-punched fabrics made of synthetic polymers such as polyvinylidene fluoride (PVDF), polyesters (PET, PLLA PLGA), polypropylene (PP) and nylon (PA) fibres have been studied for the attachment and proliferation of cell types, including mesenchymal stromal cells, mouse fibroblasts and hepatocytes [23–25]. This technique was also demonstrated to successfully produce fabrics from materials with improved bioactivity: a needle-punched scaffold made of collagen has been investigated for cartilage tissue engineering [26]. Furthermore, a needle-punched calcium alginate (CaAlg) mesh was integrated with carboxymethyl chitosan hydrogel to produce an acellular composite wound dressing [27].

The reactive printing of biomaterials using intersecting droplets is a recent development that is gaining research interest. Inkjet-based reactive printing systems were used to produce alginate hydrogels with various geometries [28–30]. A microvalve bioprinting system called reactive jet impingement (ReJI) was introduced for the fabrication of high-cell-density hydrogels [31]. The droplet-based nature of the hydrogel manufacturing process using reactive printing techniques brings an unexplored opportunity to deposit hydrogels onto substrates with different surface topographies; it can enable the fabrication of composite structures for a wide range of tissue engineering applications.

The present study is the first to integrate a nonwoven needle-punched fabric, used as a printing substrate, with ReJI bioprinting to develop a method for fabricating laminar tissue precursors. Using this strategy, biologically functional cell–hydrogel–microfibre composite constructs are manufactured, which consist of fibroblasts embedded in a collagen–alginate–fibrin hydrogel [32] and calcium alginate microfibres. Then, the cell adhesion, organisation, proliferation and ECM deposition by fibroblasts inside the constructs are evaluated in vitro. The microfibres serve as a structural substrate for the cell's migration from the hydrogel, their infiltration and the ECM deposition on the fibres. Here, we demonstrate that ReJI bioprinting can offer an efficient approach to create highly functional cell–hydrogel–microfibre composite tissue precursors, particularly for wound healing and skin tissue engineering applications.

Materials and methods

Fabrication and characterisation of calcium alginate meshes

Fabrication

The manufacture of nonwoven CaAlg was carried out by an industrial supplier, and it involved a three-step process of fibre formation, dry-laid web formation and needle punching to produce a mechanically bonded nonwoven fabric. Firstly, alginate was wet spun into continuous filaments by mixing sodium alginate with deionised water, and the created dope (5–10 wt%) was spun into a polyvalent ion calcium salt-based coagulation bath. The continuous alginate filaments solidified through solvent exchange as the water was driven off in the coagulation bath. The sodium was exchanged with calcium in the bath, resulting in water-insoluble CaAlg filaments. Before stapling (cutting) the continuous CaAlg filaments into fibres of lengths between 45 and 60 mm, the filaments were drawn in an atmosphere of steam, washed with water and dried.

The as-spun stapled CaAlg fibres were used as feedstock for dry-laid nonwoven web formation and bonding to yield a needle-punched fabric. The process involved worker–stripper carding of the fibres, consisting of progressive mechanical fibre disentanglement, inter-fibre mixing and the continuous formation of a fibrous sheet-like structure. The latter is referred to as a web, which was then cross-lapped to make a thicker structure before being mechanically bonded by needle punching. The needle punching step involved the high-speed oscillation of barbed needles vertically through the layered webs of alginate fibres to induce fibre entanglement, which enabled the production of a fully integrated and coherent CaAlg mesh.

The fabricated fibrous substrates were UV-sterilised before subsequent cell culture experiments.

Attenuated total reflectance Fourier transform infrared spectrometry

The fibrous CaAlg mesh was subjected to attenuated total reflectance Fourier transform infrared (ATR-FTIR) spectroscopic analysis on a PerkinElmer Frontier spectrophotometer using the Universal ATR accessory Single Reflection Diamond (PerkinElmer, USA), followed by evaluation through Spectrum 10 software (PerkinElmer, USA). The material was placed on the ATR crystal and pressed by a pressure clamp positioned above the crystal to allow optimal contact between the material and the crystal. The spectra of 32 scans were collected at 4 cm^{-1} over the range of $4000–550 \text{ cm}^{-1}$.

Fibre-based substrate morphology and surface profilometry

The morphology of the prepared CaAlg mesh was observed using a scanning electron microscope (Tescan Vega LMU Scanning Electron Microscope, UK). The samples were mounted on an aluminium stub using carbon tape and then gold-coated using a sputter coater (Polaron SEM Coating Unit, UK). Imaging was performed while applying 8.0 kV voltage and varying magnification. Fibre diameter was measured based on the captured SEM microphotographs using ImageJ software. The average values were calculated by collecting 30 measurements on three different microphotographs. Furthermore, an Alicona optical 3D measurement system (InfiniteFocusSL, Alicona Bruker, Germany) was used to measure surface roughness (R_a), and the data were processed by the built-in software. The view area was 4×4 mm, and 10 measurements were taken per sample ($n = 5$).

Swelling behaviour and Ca²⁺ release

CaAlg mesh samples ($15 \times 15 \times 2.5$ mm) were immersed in Dulbecco's phosphate-buffered saline (DPBS) without calcium and magnesium (Sigma-Aldrich) to evaluate their swelling behaviour over 24 h at 37 °C. At given time points $(1, 2, 4, 6, 24$ h), the samples ($n = 6$) were gently wiped with Kimtech wipes (Kimberly-Clark Professional) and weighed (w_w). The sample swelling degree ($S_w\%$) was calculated according to the following equation:

$$S_w\% = \frac{w_w - w_d}{w_d} \times 100,$$

where w_d denotes the weight of the sample before incubation in DPBS.

Another set of samples was used to assess the calcium ion release from the meshes to the solution at the abovementioned time points. A Colorimetic Calcium Detection Kit (ab102505, Abcam) was used for this purpose, and the reaction wells with samples and standards were set up following the manufacturer's protocol. The sample absorbance (at OD $= 575$ nm) was measured after 10 min of incubation with protection from light using a FLUOstar® Omega microplate reader (BMG Labtech, Germany). A standard colourimetric curve at the range from 0 to 2 μg/well was used to calculate Ca²⁺ concentration as per the manufacturer's guidelines. The results were reported as mean $\pm$ standard deviation.

Cell culture

Neonatal Human Dermal Fibroblasts (Neo-NHDF, Lonza) were used in passages $9 - 10$. The cells were cultured in high-glucose (4.5 g/L) Dulbecco's modified Eagle medium (DMEM, ThermoFisher) containing L-glutamine

and 110 mg/L pyruvate and supplemented with 10% foetal bovine serum (FBS, ThermoFisher Scientific) and 5000 U/mL penicillin/streptomycin (P/S, Sigma-Aldrich).

After bioprinting, the cell-laden constructs were cultured in the same DMEM formulation, which was changed every 2 days.

Preparation of bioinks

The collagen–alginate–fibrin (CAF) hydrogels were originally developed by Montalbano et al. [32]. The preparation protocol of CAF hydrogel precursors (pre-CAF bioink and cross-linking bioink) for the bioprinting was adapted from Ribeiro et al. [31]. Briefly, 37.5 mg of fibrinogen (from bovine plasma—Type I-S, 65–85% protein, Sigma-Aldrich) was dissolved per 1 mL of DPBS at 37 °C by gentle agitation. Sodium alginate (NaAlg, Sigma-Aldrich) was also dissolved in DBPS at 50 °C while stirring until the complete dissolution of NaAlg powder to obtain a 25 mg/mL NaAlg solution. The fibrinogen and NaAlg solutions were slowly mixed using a pipette; then, 6 mg/mL pepsin-soluble collagen solution in HCl (Collagen Solutions) was slowly added while mixing carefully. The materials were blended in a ratio of 1:2:8 of collagen:alginate:fibrinogen. This composition had a final fibrinogen concentration of 27.27 mg/mL, alginate of 4.54 mg/mL and collagen of 0.54 mg/mL, and it served as a pre-CAF bioink. To obtain a cross-linking bioink, a 500 U/mL thrombin (40–300 NIH units/mg protein, Sigma-Aldrich) solution was prepared in high-glucose DMEM with 0.1% of calcium chloride ($CaCl_2$, Sigma-Aldrich). After pelletisation, the cells were resuspended in a cross-linking bioink to obtain the desired cell printing densities. In the experiments, 5×10^6 and 30×10^6 of neo-NHDF cells were suspended per 1 mL of the cross-linking bioink.

Bioprinting process

The reactive jet impingement system consists of an in-house developed printhead integrated with a JetLab 4 XL (MicroFab Technologies, USA) printing workstation (Fig. 1) [33]. Two solenoid microvalves (nozzle diameter 500 μm, INKX0514950A, The Lee Company, USA) are mounted on the printhead and positioned to jet liquid bioinks at one another in mid-air, where they react and form a gel that lands on the substrate. Each valve is connected to a spike-and-hold drivers (The Lee Company, USA) that control the opening and closure of the valves, the bioink loading reservoirs and the pneumatics controller CT-PT4 (MicroFab Technologies, USA).

The actuation of valves was achieved by converting the JetDrive® waveform output into a signal recognisable by valves using the spike-and-hold drivers. The additional power source required for actuation was supplied by an external power supply (ISO-Tech, UK) connected to the spike-and-hold drivers, providing 24 and 3.2 V of spike voltage and hold voltage, respectively. The jet set-up parameters were programmed in the Jetlab® software. The electrical impulse in the form of a rectangular waveform with an amplitude of 3.2 V, a dwell time of 800 μs, and an actuation signal frequency of 400 Hz was applied to eject droplets simultaneously. The printing on the fly velocity (corresponding to the printhead speed) was set to 35 mm/s. The jetting pressure was set on the standalone pneumatics controller to be in the 390–400 and 420–430 mmHg range for the cross-linking bioink and pre-CAF bioink, respectively, to achieve reliable and accurate bioink deposition. To minimise cell sedimentation, an agitation system consisting of a small sterile magnet (3 mm diameter, 2 mm thick) in the reservoir with the cross-linking bioink provided a continuous gentle mixing of the bioink with cells. The magnet was controlled by an electronic motor system (applied voltage of 3.2 V) driven by the external power supply (ISO-Tech, UK).

Before and after each bioprinting experiment, the device was cleaned by a minimum of three cycles of flushing through the reservoirs, tubing and valves. A flushing cycle was defined as sequential flushes of 2 mL of each the following: trypsin, sterile-filtered deionised water, 1% Micro-90 cleaning solution, filtered 70% ethanol and a final flush of sterile-filtered deionised water through the system.

The bioprinted 3D hydrogel structures were achieved by coding and loading a script into the Jetlab® software. The desired shape, dimension of an array of droplets and number of deposited layers in the printed structures were defined in the printing script. A 7×7 pixel array of droplets with $dx = 1$ mm and $dy = 1$ mm (referring to the spacing of pixels in the x and y directions) with 7 subsequently deposited layers of the array of droplets on top of each other produced hydrogel structures with dimensions of $7 \times 7 \times 1.5$ mm (around 70 μL in volume).

The Z distance between the printhead and the printing stage was controlled in the script to 1 mm accuracy, and it was set to provide an initial 5 mm distance between the nozzles and the printing substrate. The Z distance was programmed to increase by 3 mm after every three deposited layers. The hydrogels were directly jetted onto fibrous substrates ($15 \times 15 \times 2.5$ mm) or 2D cover glass substrates (13 mm in diameter, Agar Scientific, UK). The substrates were kept dry before bioprinting. The overall hydrogel printing time was 73 s.

Biological characterisation of composite scaffolds

Cytotoxicity assay

A Live/Dead® Viability/Cytotoxicity Kit (ThermoFisher Scientific) was used to assess cell viability according to the manufacturer's guidelines. The cell media was aspirated, and
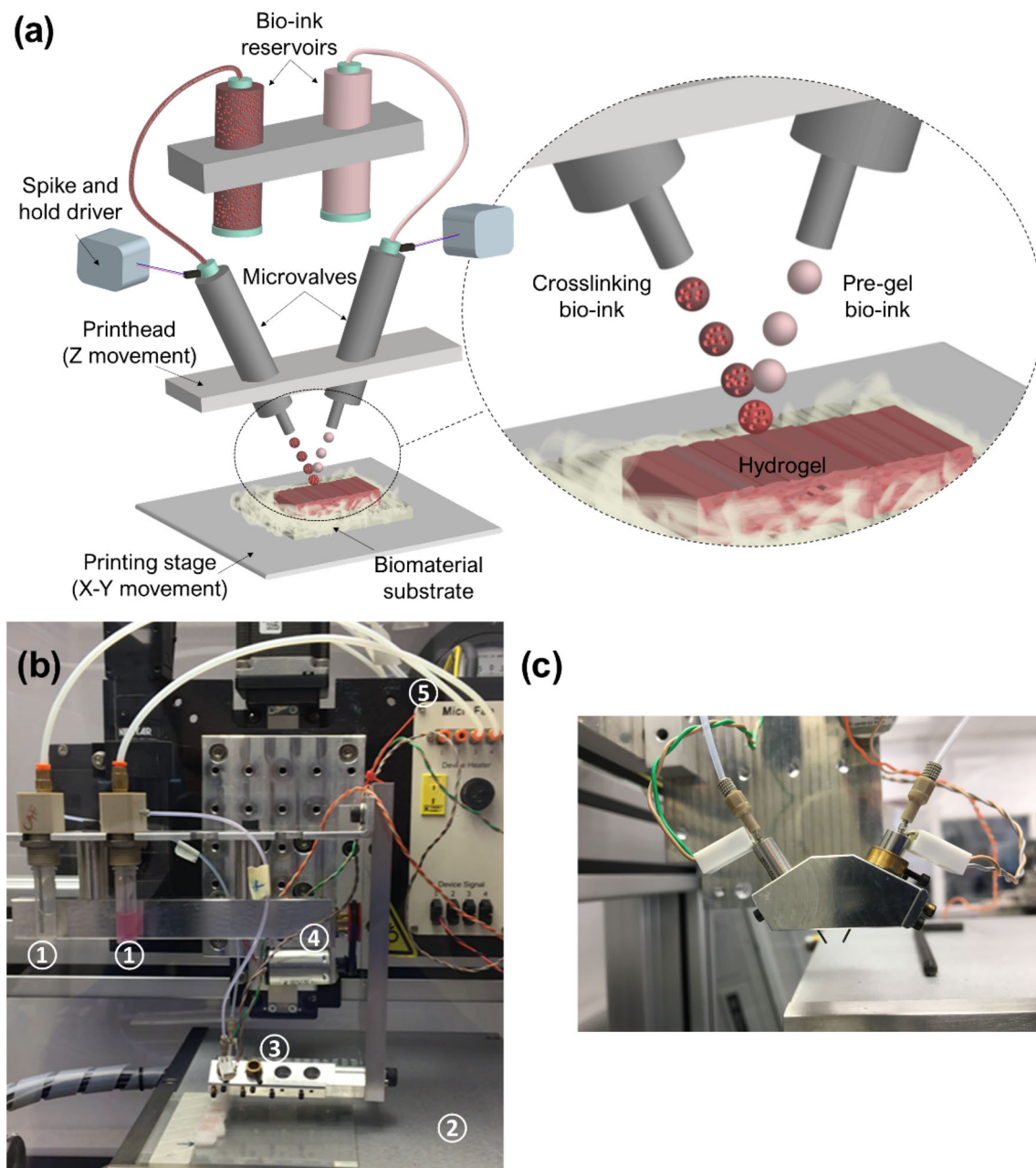
Fig. 1 Reactive jet impingement set-up. **a** ReJI schematic: the ReJI system jets bioink materials using microvalves mounted in the custom-designed printhead that is integrated with a commercial JetLab 4 XL printer. The microvalves are connected to different bioink reservoirs and directed to jet bioink droplets at one another in mid-air, where they react and form a gel that lands on the substrate of interest. Each microvalve is attached to the spike-and-hold drivers allowing for its opening and closing movement, and also connected to the pneumatic system and the printer input. **b** ReJI components: (1) Bioink reservoirs; (2) Printer stage; (3) Printhead with valves; (4) Motor system responsible for cell agitation; (5) Pressure tubing system. **c** ReJI printhead with a pair of microvalves

the samples were washed with DPBS and incubated in the Live/Dead® working solution (1 µM calcein acetoxymethyl and 4 µM EthD-1 in DPBS) at room temperature under light-protected conditions for 30 min. The constructs were imaged using an inverted confocal microscope (Nikon A1R, Japan) at 4 × magnification and captured using the equipped software (NIS-Elements). The images were taken from the top view and at the central point of the samples.

Metabolic activity assay

A PrestoBlue® assay (ThermoFisher Scientific) was conducted to evaluate the effect of printing substrate type and printed cell density on the metabolic activity of fibroblasts in the hydrogel–microfibre and hydrogel–coverglass constructs (controls) on days 1, 3 and 7. After the removal of cell media, 1 mL of PrestoBlue® working solution was added to the

samples. This solution was prepared by the addition of 10% (v/v) PrestoBlue® reagent to the cell culture media. The samples were incubated for 30 min at 37 °C under light protection. Then, 100 µL of the working solution from each sample's well was transferred to a 96-well plate, and the fluorescence was read (with excitation and emission filters of 544 and 590 nm, respectively) using a FLUOstar® Omega microplate reader (BMG Labtech, Germany). Three samples were evaluated at each time point, and each sample was measured in triplicates.

Cell proliferation assay

Cell proliferation was investigated by quantifying the DNA content in each construct using the Quant-iT Pico Green dsDNA Assay (Invitrogen). On days 1, 3 and 7, the constructs were washed with DPBS, moved to fresh well plates and then frozen at − 80 °C. Upon sample thawing, 2 mL of a digestion cocktail consisting of 100 µg/mL of proteinase K (Meridian Bioscience) and 0.1% Triton X-100 in ddH$_2$O was added to each well. The samples were incubated overnight at 37 °C to digest the hydrogel matrices and lyse the cells. Next, the sample lysate was diluted at 1:10 in TE buffer, 100 µL of the diluted sample lysate was mixed with 100 µL of PicoGreen solution, and this was incubated for 10 min under light protection and measured (with excitation and emission filters of 485 and 520 nm, respectively) in a 96-well plate using a FLUOstar® Omega microplate reader (BMG Labtech, Germany). The DNA standards were prepared according to the manufacturer's protocol. Three samples were evaluated at each time point, and each sample was measured in triplicates.

Immunofluorescence staining

The samples were fixed at different time points (immediately after printing, and 1, 3 and 7 days post-printing) using 4% paraformaldehyde solution and stored at 4 °C overnight. The cell media was aspirated before fixation, and the samples were washed with DPBS. The staining process began with permeabilising the sample (2 × 10 min) with 0.1% (v/v) Tween 20 in DPBS. This step was followed by incubation (30 min) in 2% (w/v) bovine serum albumin (BSA) in DPBS at room temperature. Next, a primary antibody, anti-vinculin (ab129002, Abcam, UK), was added to 2% BSA (Merck) to obtain a solution at 1:100 ratio, in which the samples were incubated for 1 h at room temperature. The subsequent staining steps were conducted under light-protected conditions at room temperature. The samples were washed with 0.1% DPBS/Tween 20, and a secondary antibody, Goat Anti-Rabbit Alexa Fluor® 488 (ab150077, Abcam, UK) in 0.1% DPBS/Tween 20 (1:1000 solution) was added for 1 h. The samples with Alexa488 solution were washed with 0.1% DPBS/Tween 20 and then incubated with

phalloidin-tetramethylrhodamine B isothiocyanate peptide (ThermoFisher, UK) and 0.1%DPBS/Tween 20 (1:250 solution) for another hour. Then, 4,6-diamidino-2-phenylindole solution (DAPI; 1:2500 solution, Sigma-Aldrich, UK) was added to the samples for 20 min. The images of constructs were captured using an inverted confocal microscope (Nikon A1R, Japan), equipped with a 20 × lens and NIS-Elements software.

Scanning electron microscopy

The samples were collected on days 1, 3 and 7 after printing. After collection, the cell media was aspirated, and the samples were washed with DPBS, fixed using 4% paraformaldehyde solution (ThermoFisher Scientific) and stored at 4 °C overnight. The samples were then washed with DPBS and dehydrated in successive washes in graded ethanol solutions (25, 50, 75 and 100%). The fixed and dehydrated samples were critical point dried in a Baltec Critical Point Dryer (Leica Geosystems Ltd.), mounted on an aluminium stub using carbon tape and then gold-coated using a sputter coater (Polaron SEM Coating Unit, UK). Imaging was conducted using a Tescan Vega LMU Scanning Electron Microscope (Tescan, UK) with an applied voltage of 8.0 kV under varying magnification.

Histology

Samples on days 1, 7, 14 and 21 were fixed in 10% formalin (ThermoFisher) for 24 h, transferred to histology cassettes, dehydrated in graded solutions of ethanol (70, 80, 95 and 100% EtOH) for 30 min each and cleared via immersion in xylene (ThermoFisher). The samples were then paraffin-embedded and used to prepare vertical cross Sects. (10 µm). The sample cross sections moved onto slides were deparaffined and rehydrated before haematoxylin–eosin (H&E staining). Subsequently, they were incubated in Mayer's haematoxylin (Sigma-Aldrich) and eosin solution (Sigma-Aldrich). Following H&E staining, the samples were dehydrated in graded ethanol solutions, cleared in xylene and mounted in DPX Mountant for histology (Sigma-Aldrich). The visualisation of samples was performed using an EVOS™ Microscope M5000 Imaging System (Invitrogen™, UK) at 10 × magnification.

Statistics

Statistical analysis was performed using GraphPad Prism 9 software. The quantitative data were expressed as mean ± standard deviation. The groups were analysed by two-way ANOVA with Tukey multiple comparisons test using levels of statistical significance of $p < 0.05$ (*), $p < 0.01$ (**) and $p < 0.001$ (***).
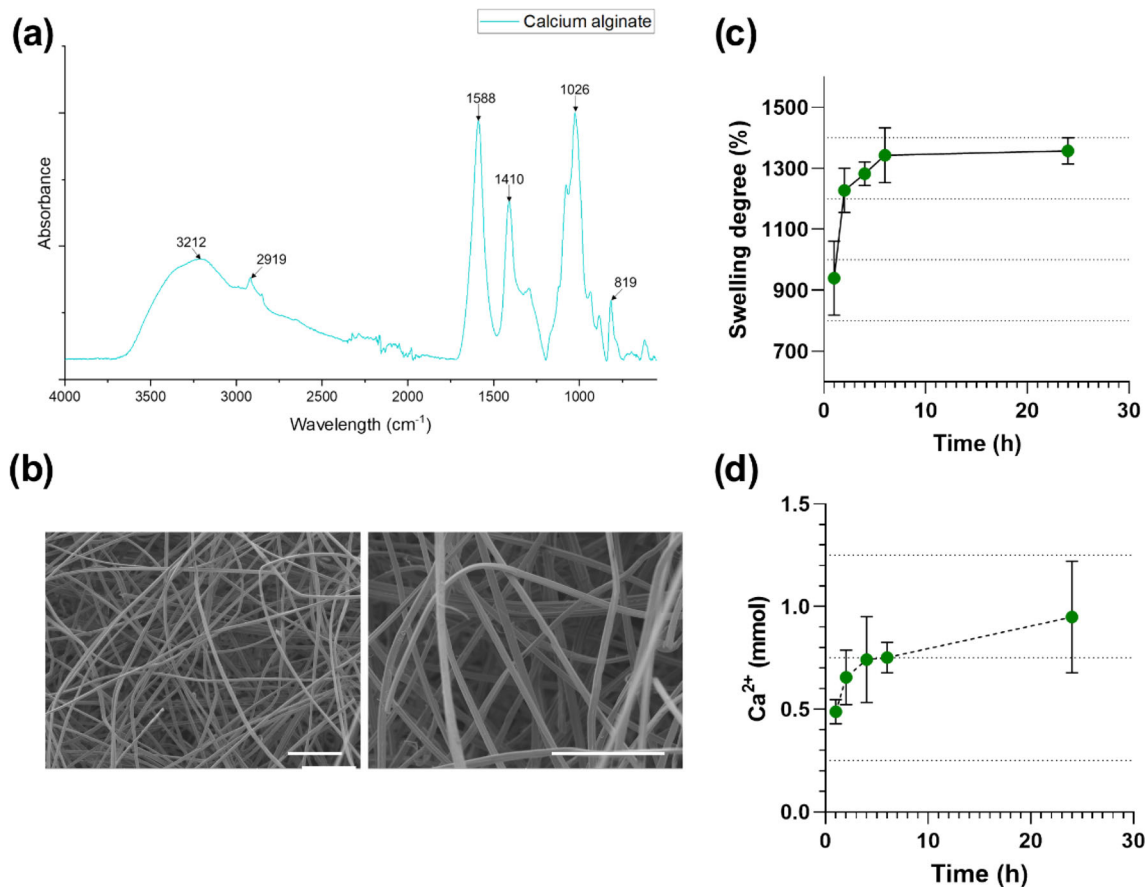
Fig. 2 **a** ATR-FTIR spectra of CaAlg. **b** SEM microphotographs of CaAlg samples at different magnifications ($200\times$ and $500\times$). Scale bar: $200\,\mu m$. **c** Swelling degree of CaAlg samples in DPBS. **d** Concentration of Ca^{2+} ions released from CaAlg samples into DPBS. Data are represented as mean $\pm$ SD

Results

Physicochemical properties of the calcium alginate mesh

The ATR-FTIR spectra of the CaAlg mesh are shown in Fig. 2a. The broad peak at 3212 cm^{-1} was attributed to the stretching vibrations of the hydroxyl group and the peak at 2919 cm^{-1} to stretching vibrations of aliphatic C–H. The peaks at 1598 cm^{-1} and 1404 cm^{-1} corresponded to the asymmetrical and symmetrical stretching vibrations of carboxylate salt ion, respectively [34]. Furthermore, the spectra of CaAlg exhibited peaks at 1026 cm^{-1} (the C–O stretching vibration) and 819 cm^{-1}, which confirmed the presence of guluronic acid, mannuronic acid and o-acetyl ester, the building blocks of alginic acid [35].

The mesh substrate obtained after the needle punching process of fibres had a thickness of around 2.5 mm with an average fibre diameter of $12.0 \pm 1.8\ \mu m$ and average roughness (R_a) of $73.5 \pm 15.0\ \mu m$. The mesh morphology before immersion in a liquid is shown in Fig. 2b. The swelling degree of the CaAlg substrates is shown in Fig. 2c. The CaAlg meshes showed high liquid absorption capacity with a quick rise in the swelling degree (above 900%) after 1 h of incubation, followed by a slower increase at the later time points, and stabilisation after 24 h.

The release of calcium ions from meshes to the solution showed a similar trend (Fig. 2d) to that of the swelling behaviour. The Ca^{2+} concentration increased quickly after 1 h to around 0.5 mmol, followed by the further release of Ca^{2+} until 24 h but at a slower rate.

Cytocompatibility, metabolic activity and cell proliferation

An overview of the produced composite constructs obtained by SEM observations is shown in Fig. 3a. The cells were largely viable on day 1 post-printing, and this high viability was retained until day 7, with few visible dead cells regardless of the printed cell density (Fig. 3b).
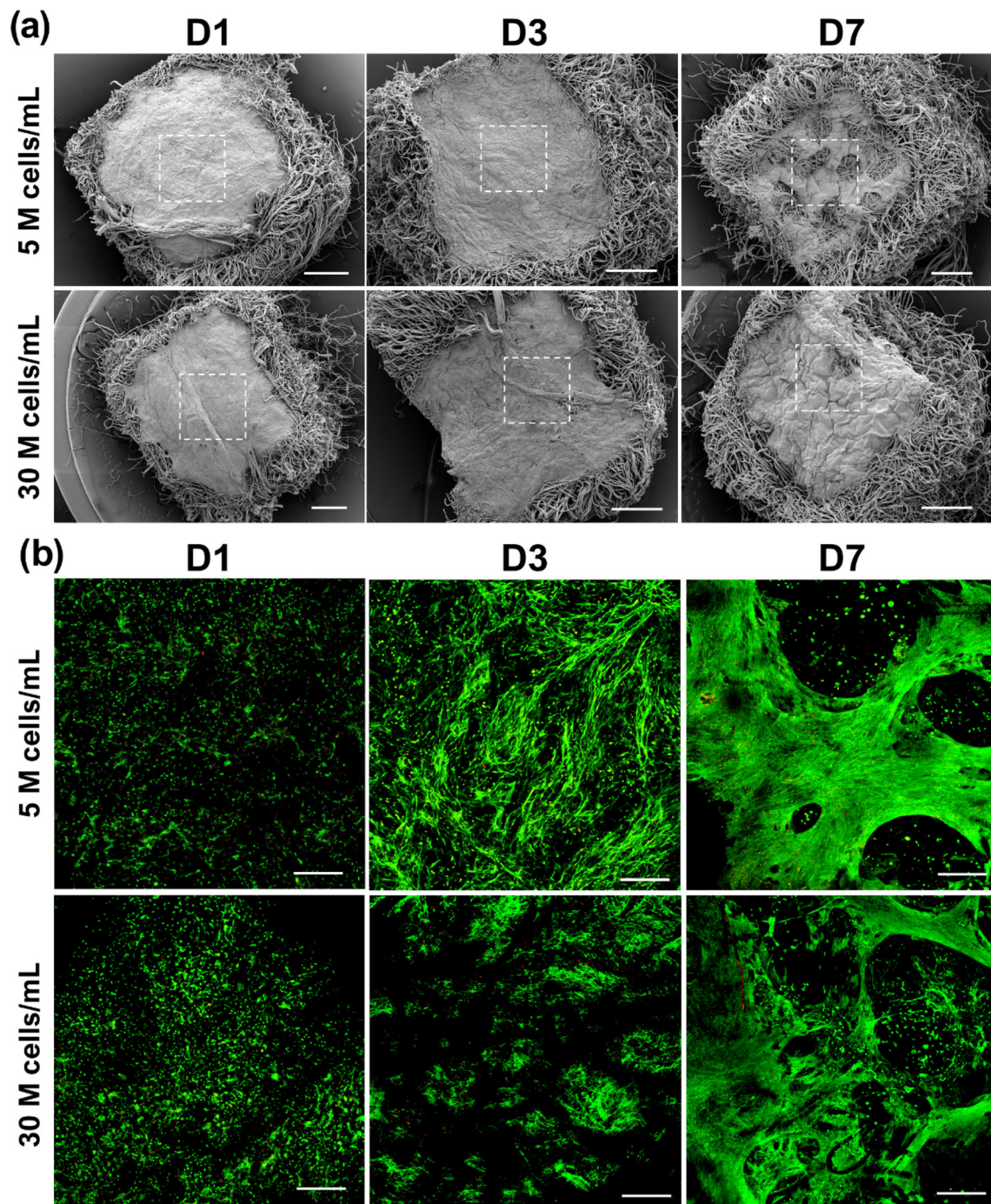
Fig. 3 **a** Overview of composite constructs illustrated based on SEM observations. Cell-laden hydrogels were directly printed onto the fibrous meshes. A white square indicates an estimated area where the Live/Dead images from Fig. 3b were taken. **b** Live/Dead staining of Neo-NHDF cells in a hydrogel printed onto a mesh on days 1, 3 and 7 for 5 M cells/mL and 30 M cells/mL nominal printed cell densities. The green staining indicates live cells, and the red staining indicates dead cells. Scale bar: **a** 1 mm, **b** 500 µm
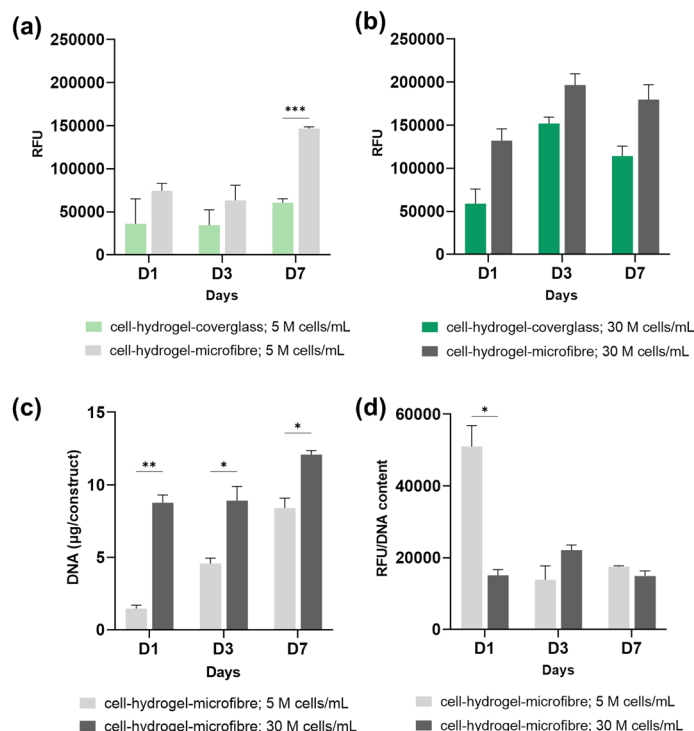
Fig. 4 Metabolic activity of Neo-NHDF cells in hydrogel printed onto a mesh and a cover glass at the nominal **a** 5 M cells/mL and **b** 30 M cells/mL printed cell densities. **c** DNA quantification of Neo-NHDF cells in the cell–hydrogel–microfibre constructs. **d** Metabolic activity of Neo-NHDF cells in hydrogel printed onto a mesh normalised to the total DNA content per construct. Data are represented as mean ± SD ($n = 3$); $^{***}p < 0.001$; $^{**}p < 0.01$, $^{*}p < 0.05$

Figure 4a shows no significant differences in metabolic activity between day 1 and day 3 when printing was performed onto a mesh or a coverglass substrate at the nominal 5 M cells/mL cell density. On day 7, the metabolic activity of fibroblasts was significantly higher in the hydrogel–microfibre constructs compared to the hydrogel–coverglass constructs ($p < 0.001$). Conversely, for the nominal 30 M cells/mL printed cell density, the fibrous samples promoted a significantly higher cellular metabolic activity ($p < 0.05$) than the coverglass samples on the days of measurement (Fig. 4b).

Figure 4c shows that the DNA content of the constructs with the nominal 30 M cells/mL printed cell density (8.76 ± 0.53 μg) was about six times higher than that for the 5 M cells/mL printed cell density equivalents (1.46 ± 0.24 μg). A nearly threefold increase in the amount of DNA in was observed in the 5 M cells/mL constructs (4.56 ± 0.37 μg) by day 3. This was followed by a further approximately twofold increase in the DNA content (8.39 ± 0.68 μg) by day 7. On the other hand, the 30 M cells/mL constructs showed less pronounced cellularity changes. From days 1 to 3 (8.90 ± 0.98 μg), the DNA content remained almost constant, and about 1.35-fold increase was noted between day 3 and day 7 (12.08 ± 0.29 μg). The initial sixfold change between the

constructs with two different nominal printed cell densities decreased to about 1.5 by day 7. In addition, the DNA content in the 5 M cells/mL constructs on day 7 equalled the initial DNA content measured on day 1 in the 30 M cells/mL constructs.

Figure 4d shows that the printed cell density seemed to influence the metabolic activity only on day 1 when the 5 M cells/mL cell–hydrogel–microfibre constructs yielded significantly higher values ($p < 0.05$) of metabolic activity than the 30 M cells/mL constructs.

Cell morphology and distribution, and cell–cell and cell–biomaterial interactions

After printing onto the fibrous substrate, fibroblasts had a typical rounded morphology and were distributed in the hydrogel matrix without a particular organisation on day 0 (Fig. 5). The images of constructs with the nominal 30 M cells/mL printed cell density showed a higher number of cells present within the same volume. On day 1, most of the cells were elongated, and they started to interact with each other. Some single rounded cells were distributed in constructs with the nominal 5 M cells/mL printed cell density, while the 30 M cells/mL constructs already showed higher
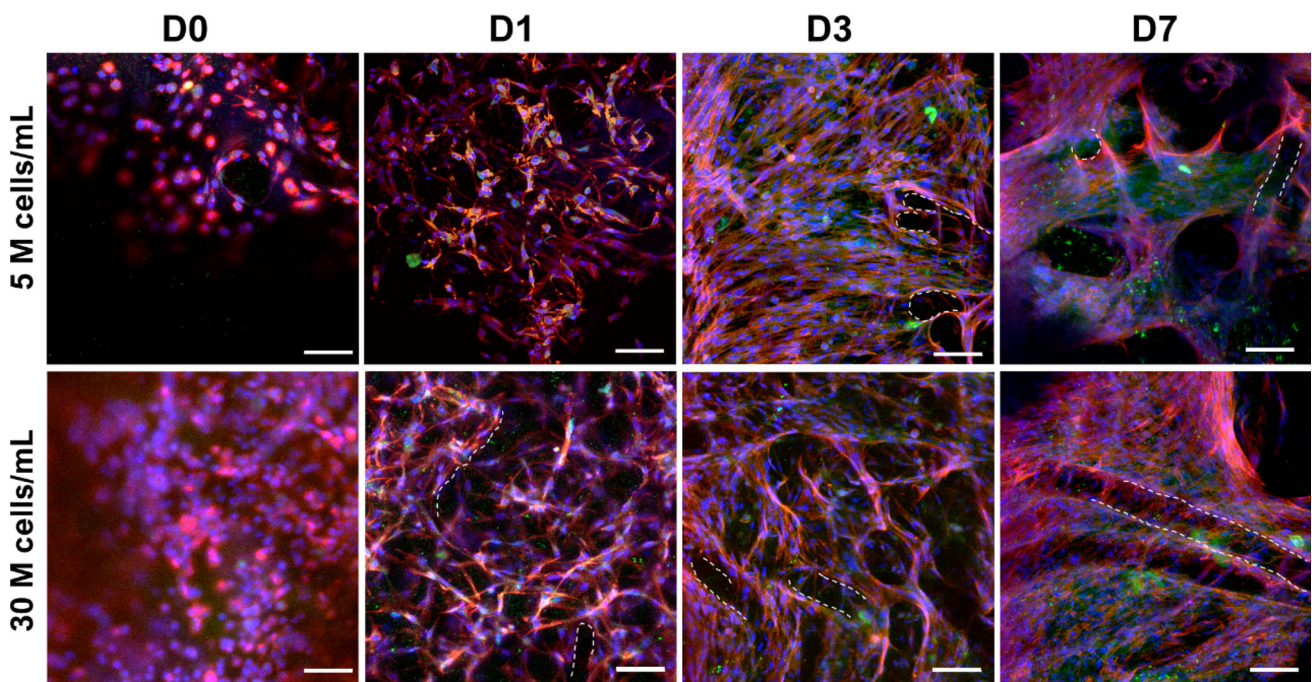
Fig. 5 Confocal observations of Neo-NHDF cells in a hydrogel printed onto a mesh on days 0, 1, 3 and 7, for 5 M cells/mL and 30 M cells/mL nominal printed cell densities. Blue, red and green staining respectively indicates the cell nuclei, F-actin and vinculin (focal adhesion plaques). The white lines indicate the cell-laden hydrogel organisation being influenced by fibres. Scale bar: 100 μm

organisation with close cell-to-cell interactions and initial distribution around the fibres. On day 3, the structural organisation inside the construct became more explicit for the 30 M cells/mL samples (Fig. 6). Nevertheless, confocal observations of the 5 M cells/mL composite constructs indicated that cell–fibre interactions also determine cell organisation, but this process implies progress at a slower rate. On day 7, both types of constructs showed highly dense tissue-like formation.

As shown in the SEM microphotographs (Fig. 7), cells on the top surface of bioprinted hydrogels could be observed on day 1, but most cells were embedded in the matrix. The cells then gradually migrated outside of the hydrogel and interacted with the fibres. On day 7, dense tissue-like layers covered the top surface. The bioprinted CAF hydrogel resembled the native fibroblast ECM from day 0, making it difficult to distinguish between the CAF matrix and the ECM produced by cells. The SEM observations in Fig. 8a indicate that the CAF matrix was densely cross-linked on day 1, with no nanofibrous deposits visible on the CaAlg fibres. By day 7, a new form of matrix deposits with loose and nanofibrous morphology was seen on the pristine CaAlg fibres, suggesting new ECM deposition and/or the disentangling of cross-linked CAF by fibroblasts.

The construct cross sections stained with hematoxylin and eosin (H&E) demonstrated cellular migration and infiltration into the 3D microfibrous network. The stainings also corroborated the SEM observations, demonstrating the ECM production by fibroblasts.

Eosin stains proteins nonspecifically in varying intensities of pink. The bioprinted hydrogel matrix was composed of collagen and fibrin, and it was stained bright pink, whereas fibroblasts embedded in the gel were represented by their purple nuclei. From day 7, different intensities of pink stains were observed, representing the cell cytoplasm and deposited ECM. The hydrogel borders were visible on day 1, but after 7 days, a dense tissue layer replaced the hydrogel matrix, and the cells were more dispersed in the constructs. Based on the H&E images, the depth of cellular infiltration oscillated around 1.2–1.4 cm. The CaAlg fibres were not stained by H&E, or some seemed to stain faded pink. The presence of cells inside the constructs was demonstrated over three weeks of cell culture (Fig. 8b).

Discussion

Nonwoven production can be used as a scalable alternative technique to electrospinning in tissue engineering

Weaving, knitting, braiding and nonwoven production, including electrospinning, are techniques for fabricating
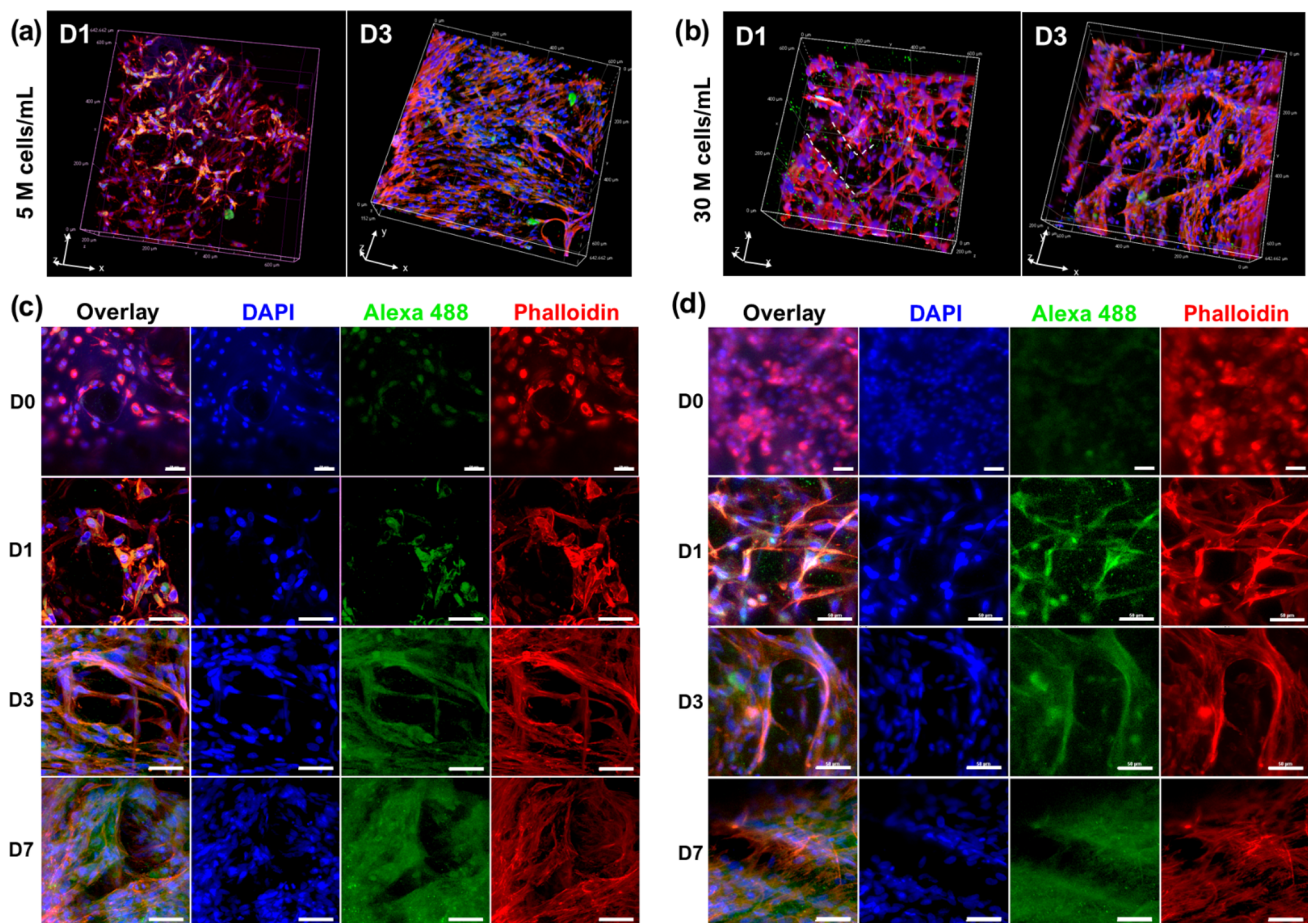
Fig. 6 Z-stack projection of the organisation of Neo-NHDF cells on day 1 and day 3 for **a** 5 M cells/mL and **b** 30 M cells/mL printed cell densities; Confocal observations of the Neo-NHDF cells in a hydrogel printed onto a mesh on days 0, 1, 3 and 7 for **c** 5 M cells/mL and **d** 30 M cells/mL nominal printed cell densities, showing cellular morphology alongside the fibres. Blue, red and green staining respectively indicates cell nuclei, F-actin and vinculin. Scale bar: **a**, **b** 100 μm; **c**, **d** 50 μm

fibre-based scaffolds [22, 36]. Amongst them, electrospinning has been recognised as the most popular choice in tissue engineering; its widespread use is attributed to the cheap and accessible set-up, ease of manipulation and versatility [37]. However, electrospinning technology can be challenging in terms of scaling up and the ability to manufacture thick (> 1 mm) high-porosity substrates (> 80%). In this research, an alternative nonwoven production route was investigated, which is already industrially deployed, e.g. for the production of chronic wound dressings. The manufacture of nonwovens is easily scalable due to its cost-effectiveness and high productivity thanks to the elimination of the yarn manufacturing step (which is involved in the fabrication of other textile scaffolds, such as woven or knitted fabrics).

Electrospun scaffolds are characterised by nanometre-scale fibres and a high surface area, which makes them topographically similar to native ECM, supporting cell attachment, spreading and proliferation. However, the subcellular pore size between nanofibres results in cell adhesion

to the outer surface and limited infiltration into the structure, which in turn can lead to the nonoptimal integration of electrospun scaffolds with deposited cells and in turn slow the regeneration process [14]. In this research, the microfibres obtained using nonwoven production were considerably coarser than the electrospun nanofibres previously reported for tissue engineering applications. The average fibre diameter of the produced mesh was around 12-fold higher (about 12 μm) than the electrospun fibres reported elsewhere (range of 0.5–1.5 μm) [38–40]. The high roughness of the mesh substrates confirmed their 3D architecture. On the contrary, the 3D architecture of electrospun scaffolds remains disputable as their thickness is low, thus the fabrication of bulk 3D structures is challenging [41, 42].
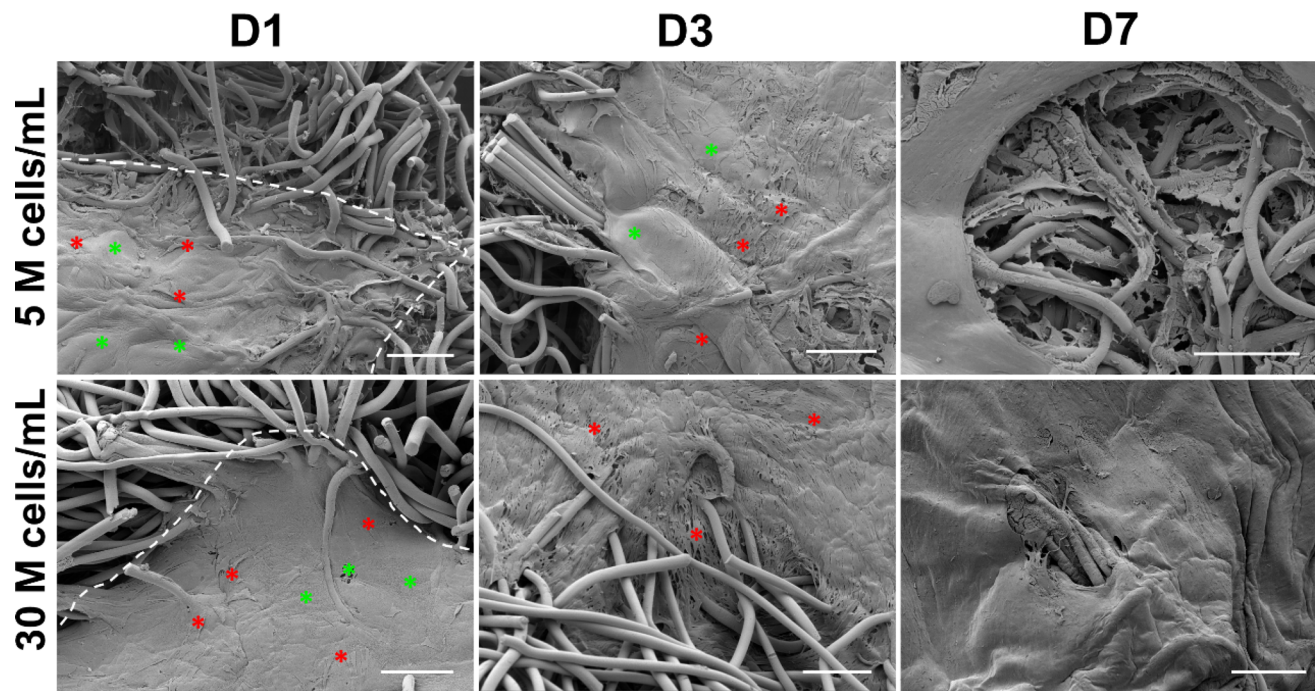
Fig. 7 SEM microphotographs of composite constructs showing cell–hydrogel–fibre interactions on days 1, 3 and 7 for 5 M cells/mL and 30 M cells/mL nominal printed cell densities. The red and green stars indicate exemplary areas of constructs pointing out cells/cell layer and a bioprinted CAF matrix, respectively. Due to dense cell formation on day 7, it is difficult to distinguish between the cells and the hydrogel matrices. Scale bar: 200 μm

Reactive jet impingement bioprinting enables the integration of cell-laden hydrogels with microfibrous meshes

Scaffolds for tissue engineering must be porous, and the pores should create an interconnected network and be within a suitable size range to promote cell infiltration and cell–cell communication [43]. The nonwoven needle-punched scaffold fabricated in our study not only had coarse fibres but also high porosity. Such 3D structures with large pores and distance between fibres may diminish cell–cell and cell–fibre interactions, unless cells are delivered in a 3D matrix within the fibres. The nature of alginate of not possessing adhesion ligands for mammalian cells should also be appreciated [44]. The capacity to deliver cells embedded in the hydrogel matrix onto a microfibrous substrate was determined to be crucial in the design of these cell-laden composite constructs. The manufacturing strategy of a cell–hydrogel–fibre composite based on embedding cells in the hydrogel and bioprinting directly onto the mesh created a unique model, which favoured cell–cell interactions and enabled the gradual migration of cells outside the hydrogel and their infiltration into the microfibres.

The ReJI bioprinting technique has been shown as a new alternative in a portfolio of strategies to fabricate hydrogel–fibre composite scaffolds. The strategy of drop-by-drop deposition of bioinks enabled the production of spatially organised hydrogel architecture that can be deposited on the fibrous mesh despite its high surface roughness and porosity. Therefore, this strategy also eliminated the effect of filament dragging and poor adhesion of the first layer to the printing surface, commonly encountered in extrusion-based bioprinting systems. What is more, the drop-by-drop approach allowed for the homogenous distribution of cells within the hydrogel matrix at high cell concentrations, which would be challenging to achieve by casting cell-laden hydrogels.

There is a clear technological potential to scale-up ReJI as a manufacturing system. The bioinks can be concurrently deposited from multiple sets of valves to produce constructs with clinically relevant sizes. At present, using one set of valves, the fabrication of a clinically relevant construct size (e.g. 4 × 4 × 0.2 cm) takes around 50 min, and that while employing multiple sets of valves can be reduced to less than 10 min. As the ReJI process requires materials that can immediately cross-link upon impingement, the main challenge is to expand the library of bioinks compatible with the system.

The selection of nonwoven production for the fibre component of the composite adds the benefits of improved structural integrity (the fibres provided structural organisation of composite constructs, as shown in Fig. 3a), ease of handling and provides a more extensive substrate for the cells to migrate to. The shape of constructs was maintained, and the
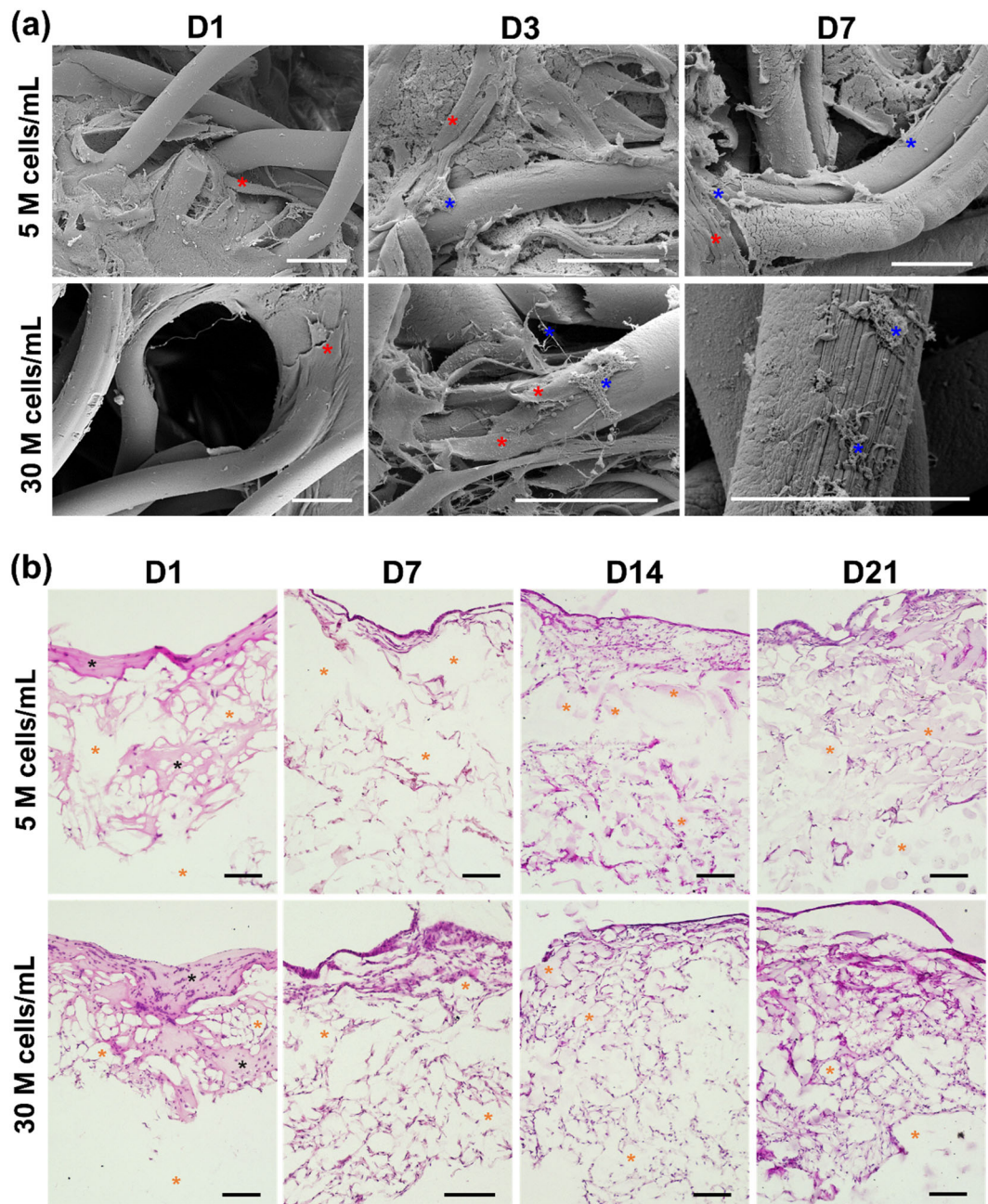
Fig. 8 a SEM microphotographs of composite constructs showing ECM deposition by neo-NHDF cells for nominal 5 M cells/mL and 30 M cells/mL printed cell densities. The red and blue stars indicate the cells and ECM deposits, respectively. **b** A histological cross section of constructs stained with hematoxylin and eosin showed cell infiltration, proliferation and ECM production after 21 days of cell culture. The black stars point out the cross-linked CAF matrix stained bright pink on day 1, and the orange stars indicate the presence of fibres/voids within the structures. Scale bar: **a** 20 μm; **b** 200 μm

cell-laden constructs were handled efficiently over the experimental period. When incubating acellular CaAlg meshes, they tended to disintegrate quickly, loose fibres were visible in the solution, and handling was no longer possible after 3 days. However, incorporating the cells into hydrogels prevented the quick disintegration of the mesh into loose fibres by reducing the available sites for ionic exchange between the fibres and the cell media. Future work will consider

evaluating the mechanical properties and morphological evolution of cellular and acellular constructs over the culture time and correlating them with handling ability.

Higher fibroblast density boosts initial cell–cell and cell–biomaterial cross talk

The metabolic activity of fibroblasts was positively influenced by the 3D substrate underneath the bioprinted hydrogel. The 3D fibrous mesh created a more complex environment, which yielded higher values of cell metabolic activity than the 2D cover glass. The higher cell density embedded in the hydrogel resulted in more pronounced initial cellular interactions. This in turn led to faster cell migration outside of the hydrogel matrix to find room for attachment and elongation (Fig. 4b). For the 5 M cells/mL composite constructs, the effect of printing substrate on the cell metabolic activity was evident by day 7 (Fig. 4a). On the other hand, the nominal printed cell density had a less apparent effect on the cell metabolic activity than the printing substrate (Fig. 4d). The initial peak in the cell metabolic activity of the 5 M cells/mL constructs could be the effect of a higher proliferation rate in the samples with initially lower number of cells. The DNA content per construct was quantified for the hydrogel–microfibre constructs (Fig. 4c). The results revealed that constructs with lower initial cell density had faster proliferation, which might suggest that the initial printed cell density was a driving factor of cellular behaviour, supporting cell proliferation in the 5 M cells/mL composite constructs and other cellular behaviour, such as cell migration and ECM production, in the 30 M cells/mL composite constructs.

From a qualitative aspect, we saw highly dense tissue-like structures formed by day 7 for both the 5 M cells/mL and 30 M cells/mL printed cell densities (Fig. 5). Meanwhile, the 30 M cells/mL constructs facilitated faster cell–cell communication and cell–fibre integration, including cellular organisation in between the fibres, higher cell infiltration and more abundant ECM production. The 3D Z-stack projections of fibroblasts show the difference in cell distribution around fibres between day 1 and day 3, indicating that cells organised faster inside the 30 M cells/mL composite constructs (Fig. 6). Adhesive interactions between cells and the surface they are attached to influence cell morphology [45]. In this work, the expression of vinculin by fibroblasts was investigated using immunofluorescence staining. Vinculin is an important focal adhesion protein involved in cell signalling, adhesion and migration localised to focal adhesions [46]. Focal adhesions are crucial for processes such as cell–substrate adhesion, cell movement and wound healing [47]. The formation of a focal adhesion involves the linkage of focal adhesion proteins like vinculin to ECM-bound integrins and binding of the ECM-focal adhesion complex to actin filaments [47]. This binding by vinculin or other focal adhesion proteins is a crucial step to forming a mechanical link between the cell and the biomaterial. The immunofluorescence staining for vinculin (Fig. 6) showed evenly distributed focal adhesions, pointing out a complex cross talk between the cytoskeleton, ECM and fibres.

As depicted by SEM observations, the CAF matrix, initially mimicking the native ECM, was replaced over time by the ECM deposited by fibroblasts (Figs. 7 and 8a). As shown by histological images, cells gradually migrated outside of the hydrogel and infiltrated into the microfibres (Fig. 8b). The resultant higher cell density facilitated a faster CAF hydrogel matrix remodelling towards native ECM, and the CaAlg microfibres provided structural support for cell migration and ECM deposition.

Cell–hydrogel–microfibre composite tissue precursors for wound healing and laminar tissue engineering applications

The post-printing dermal fibroblasts had high viability rates, which demonstrates the biocompatibility of the used biomaterials and shows that ReJI bioprinting did not compromise cell viability. Fibrin and collagen as the bioink components and alginate as the bioink and fibre component are widely used materials as scaffolds in skin tissue engineering applications [48–51]. Fibrin and type I collagen are two key ECM components that are essential to the matrix alteration in wound beds during the wound healing process. After injury, fibrinogen forms a fibrin-rich clot with thrombin, which re-establishes homeostasis [52]. Fibrin serves as a provisional matrix for an inflow of fibroblasts, keratinocytes, endothelial cells and monocytes to proliferate, organise and perform specialised functions at the site of injury, inflammation or infection [53]. Collagen is produced and remodelled by fibroblasts after their migration into the provisional matrix, and it gradually becomes the main component of ECM in healed wounds. The cells migrate to the wound bed and bind to fibrin via integrin receptors [54]. Needle-punched fibrous nonwoven fabrics made of calcium alginate have been previously used as wound dressings due to their high absorption capacity [55, 56] and anti-infective properties [57]. Calcium ions released from CaAlg meshes through ion exchange with sodium in wound exudates were shown to play a role in wound response by aiding haemostasis, coagulation in the early lesion and cell signalling [58]. The swelling behaviour depicted in Fig. 2c and the release of Ca^{2+} ions shown in Fig. 2d demonstrate that both datasets follow a similar trend, i.e. an initial sharp increase in the swelling degree (from 0 to 900%) can be correlated with the highest increase in the amount of Ca^{2+} (from 0 to 0.5 mmol) released into the solution after the same period. Upon the contact of CaAlg fibres with DPBS, the Na^+ ions present in the DPBS buffer begin to exchange with the Ca^{2+} ions chelated with alginate sequences. With the entry of more Na^+ ions, the loose macromolecular structure enlarges, causing the fibres to uptake more solution [59]. High swelling is a desirable

property of products for skin regeneration, as it helps to maintain a moist environment and absorb wound exudates.

To date, there has been no clear indication of the optimal fibroblast concentration for wound healing and skin regeneration therapies. However, when developing cell-laden constructs using bioprinting, the fibroblast density has been dictated by the technological limitations of printers. Lee et al. fabricated a bilayered skin tissue model using microvalve bioprinting with a fibroblast density of 1 M cells/mL. Higher cell concentrations induced clogging problems in the dispenser with aggregated cell pellets [60]. In another in vitro study, Daikuara et al. extruded fibroblasts embedded in a platelet lysate-based bioink at a cell density of 1 M cells/mL [61]. However, the 1 M cells/mL printed cell density did not enhance quick cell–cell communication and organisation, with fibroblasts showing a rounded morphology on day 1. Recent in vivo studies by Albanna et al. and Jorgensen et al. reported the in situ bioprinting of about 0.94 million and 20 million fibroblasts per mL, respectively [62, 63]. Both studies demonstrated that the bioprinting procedure accelerated wound closure and resulted in the formation of new skin, though the direct effect of printed cell density was not discussed. Our in vitro study indicated that cellular events progress at different rates, depending on the printed cell density. Considering the development of regenerative wound dressings, our data suggest that the number of fibroblasts delivered directly to the wound bed could accelerate some events in the wound healing cascade and ultimately influence the time required for a wound to heal completely. However, further research is needed to understand the mechanism of these dependencies in a wound healing microenvironment.

In a wider sense, skin is one of many examples of tissue with laminar structure, including multiple layers with specific roles integrated in order to produce the required function. By varying the cell/hydrogel/fibre content, the approach we describe here could have a more general application in laminar tissue engineering. Thus far, the essential technique in laminar tissue engineering has been cell sheet engineering [64], which has been investigated for a wide range of applications. Cell sheet engineering produces high-cell-density sheets of cells with ECM, but one of the main drawbacks of this approach is the time required to grow the sheets (timescale of 2–3 weeks [65]). The approach we outline here offers an alternative to the generation of high-cell-density sheets, which could operate using off-the-shelf cell sources to produce thin layers with high-cell-density, and with the fibre sheet offering the ease of handling. The practicality and potential to produce such "on demand" sheets make our overall approach an interesting one to carry forward for laminar tissue engineering.

Conclusions

In this paper, we demonstrated that the ReJI bioprinting technology is an effective and valuable strategy to fabricate hydrogel–fibre composites. Specifically, ReJI as a strategy for composite fabrication allowed for (i) A drop-by-drop deposition of spatially organised hydrogels directly onto fibres; (ii) The incorporation of cells into the composite manufacturing process; (iii) The homogenous distribution of cells at high densities. Cell–hydrogel–microfibre composite tissue precursors were produced with two different cell densities of fibroblasts (5×10^6 and 30×10^6 cells/mL, respectively). The 5 M cells/mL composite tissue precursors supported cell proliferation. In contrast, in the 30 M cells/mL composites, faster cellular migration, better organisation between fibres and the tendency of cells to produce more abundant ECM were observed. The hydrogel component formed an initial ECM-like environment supporting close cell–cell interactions, despite the high porosity and surface roughness of fibre-based substrate. The needle-punched mesh provided (i) An extensive substrate for the migration of cells from the hydrogel and subsequent ECM deposition; (ii) High structural integrity of the composite construct and ease of handling. The infiltration of fibroblasts inside the constructs and the formation of dense tissue-like layered structures suggest that cell–hydrogel–microfibre composites could mimic dermal layers. Thus, such composite tissue precursors may have potential applications as models or implants in laminar tissue engineering, e.g. as regenerative wound dressings.

Author contributions MK was involved in conceptualisation, data curation, formal analysis, methodology, investigation and writing the original draft; AMF and PG were responsible for conceptualisation, writing, reviewing and editing, and supervision; SJR took part in resources, writing, reviewing and editing; KD participated in conceptualisation, writing, reviewing and editing, supervision and funding acquisition.

Declarations

Conflict of interest The authors declare that they have no conflict of interest.

Ethical approval This study does not contain any studies with human or animal subjects performed by any of the authors.

References

1. Murphy SV, Atala A (2014) 3D bioprinting of tissues and organs. Nat Biotechnol 32:773–785. https://doi.org/10.1038/nbt.2958

2. Matai I, Kaur G, Seyedsalehi A et al (2020) Progress in 3D bioprinting technology for tissue/organ regenerative engineering. Biomaterials 226:119536. https://doi.org/10.1016/j.biomaterials.2019.119536

3. Kang HW, Lee SJ, Ko IK et al (2016) A 3D bioprinting system to produce human-scale tissue constructs with structural integrity. Nat Biotechnol 34:312–319. https://doi.org/10.1038/nbt.3413

4. Martínez Ávila H, Schwarz S, Rotter N et al (2016) 3D bioprinting of human chondrocyte-laden nanocellulose hydrogels for patient-specific auricular cartilage regeneration. Bioprinting 1–2:22–35. https://doi.org/10.1016/j.bprint.2016.08.003

5. Cidonio G, Glinka M, Dawson JI et al (2019) The cell in the ink: Improving biofabrication by printing stem cells for skeletal regenerative medicine. Biomaterials 209:10–24. https://doi.org/10.1016/j.biomaterials.2019.04.009

6. Daly AC, Pitacco P, Nulty J et al (2018) 3D printed microchannel networks to direct vascularisation during endochondral bone repair. Biomaterials 162:34–46. https://doi.org/10.1016/j.biomaterials.2018.01.057

7. Ng WL, Wang S, Yeong WY et al (2016) Skin bioprinting: impending reality or fantasy? Trends Biotechnol 34:689–699. https://doi.org/10.1016/j.tibtech.2016.04.006

8. Velasco D, Quílez C, Garcia M (2018) 3D Human skin bioprinting a view from the bio side. J 3D Print Med 2(3):141–162. https://doi.org/10.2217/3dp-2018-0008

9. Hospodiuk M, Dey M, Sosnoski D et al (2017) The bioink: a comprehensive review on bioprintable materials. Biotechnol Adv 35:217–239. https://doi.org/10.1016/j.biotechadv.2016.12.006

10. Ahmed EM (2015) Hydrogel: preparation, characterization, and applications: a review. J Adv Res 6:105–121. https://doi.org/10.1016/j.jare.2013.07.006

11. DeForest CA, Anseth KS (2012) Advances in bioactive hydrogels to probe and direct cell fate. Annu Rev Chem Biomol Eng 3:421–444. https://doi.org/10.1146/annurev-chembioeng-062011-080945

12. Zhu J, Marchant RE (2011) Design properties of hydrogel tissue-engineering scaffolds. Expert Rev Med Devices 8:607–626. https://doi.org/10.1586/erd.11.27

13. Bosworth LA, Turner LA, Cartmell SH (2013) State of the art composites comprising electrospun fibres coupled with hydrogels: a review. Nanomed Nanotechnol Biol Med 9:322–335. https://doi.org/10.1016/j.nano.2012.10.008

14. Xu S, Deng L, Zhang J et al (2016) Composites of electrospun-fibers and hydrogels: a potential solution to current challenges in biological and biomedical field. J Biomed Mater Res Part B Appl Biomater 104:640–656. https://doi.org/10.1002/jbm.b.33420

15. Shapiro JM, Oyen ML (2013) Hydrogel composite materials for tissue engineering scaffolds. JOM 65:505–516. https://doi.org/10.1007/s11837-013-0575-6

16. Ekaputra AK, Prestwich GD, Cool SM et al (2008) Combining electrospun scaffolds with electrosprayed hydrogels leads to three-dimensional cellularization of hybrid constructs. Biomacromol 9:2097–2103. https://doi.org/10.1021/bm800565u

17. Yang G, Lin H, Rothrauff BB et al (2016) Multilayered polycaprolactone/gelatin fiber-hydrogel composite for tendon tissue engineering. Acta Biomater 35:68–76. https://doi.org/10.1016/j.actbio.2016.03.004

18. Jordan AM, Kim SE, Van De Voorde K et al (2017) In situ fabrication of fiber reinforced three-dimensional hydrogel tissue engineering scaffolds. ACS Biomater Sci Eng 3:1869–1879. https://doi.org/10.1021/acsbiomaterials.7b00229

19. Malikmammadov E, Tanir TE, Kiziltay A et al (2019) Preparation and characterization of poly(ε-caprolactone) scaffolds modified with cell-loaded fibrin gel. Int J Biol Macromol 125:683–689. https://doi.org/10.1016/j.ijbiomac.2018.12.036

20. Li X, Cho B, Martin R et al (2019) Nanofiber-hydrogel composite–mediated angiogenesis for soft tissue reconstruction. Sci Transl Med 11(490):aau6210. https://doi.org/10.1126/scitranslmed.aau6210

21. de Ruijter M, Ribeiro A, Dokter I et al (2019) Simultaneous micropatterning of fibrous meshes and bioinks for the fabrication of living tissue constructs. Adv Healthc Mater 8:1800418. https://doi.org/10.1002/adhm.201800418

22. King MW, Chen J, Deshpande M et al (2019) Structural design, fabrication and evaluation of resorbable fiber-based tissue engineering scaffolds. In: Jacob-Lopes E, Zepka LQ (eds) Biotechnology and Bioengineering. IntechOpen, UK. https://doi.org/10.5772/intechopen.84643

23. Rossouw CL, Chetty A, Moolman FS et al (2012) Thermo-responsive non-woven scaffolds for "smart" 3D cell culture. Biotechnol Bioeng 109:2147–2158. https://doi.org/10.1002/bit.24469

24. Edwards SL, Russell SJ, Ingham E, et al. (2005) Nonwoven scaffolds of improved design for the tissue engineering of the anterior cruciate ligament. Medical Textiles and Biomaterials for Healthcare Inc Proceeding MEDTEX03 International Conference Exhibition Healthcare Medical Textile 2005: 355–365. https://doi.org/10.1533/9781845694104.6.355.

25. Schellenberg A, Ross R, Abagnale G et al (2014) 3D non-woven polyvinylidene fluoride scaffolds: fibre cross section and texturizing patterns have impact on growth of mesenchymal stromal cells. PLoS ONE 9:94353. https://doi.org/10.1371/journal.pone.0094353

26. He N, Ke Q, Huang C et al (2014) Needle-punched nonwoven matrix from regenerated collagen fiber for cartilage tissue engineering. J Appl Polym Sci 131(13):40404. https://doi.org/10.1002/app.40404

27. Gao Y, Zhang X, Jin X (2019) Preparation and properties of minocycline-loaded carboxymethyl chitosan Gel/Alginate nonwovens composite wound dressings. Mar Drugs 17(10):575. https://doi.org/10.3390/md17100575

28. Sakurada L, Sole-Gras M, Christensen K et al (2020) Liquid-absorbing system-assisted intersecting jets printing of soft structures from reactive biomaterials. Addit Manuf 31:100934. https://doi.org/10.1016/j.addma.2019.100934

29. Teo MY, Kee S, RaviChandran N et al (2020) Enabling free-standing 3D hydrogel microstructures with microreactiveinkjet printing. ACS Appl Mater Interf 12:1832–1839. https://doi.org/10.1021/acsami.9b17192

30. Christensen K, Compaan A, Chai W et al (2017) In situ printing-then-mixing for biological structure fabrication using intersecting

jets. ACS Biomater Sci Eng 3:3687–3694. https://doi.org/10.1021/ACSBIOMATERIALS.7B00752

31. Da Conceicao RR, Pal D, Ferreira AM et al (2019) Reactive jet impingement bioprinting of high cell density gels for bone micro-tissue fabrication. Biofabrication 11(1):015014. https://doi.org/10.1088/1758-5090/aaf625

32. Montalbano G, Toumpaniari S, Popov A et al (2018) Synthesis of bioinspired collagen/alginate/fibrin based hydrogels for soft tissue engineering. Mater Sci Eng C 91:236–246. https://doi.org/10.1016/j.msec.2018.04.101

33. Benning MJ, Dalgarno KW. (2019) WO/2019/008373 Printing Apparatus and Method

34. Jejurikar A, Seow XT, Lawrie G et al (2012) Degradable alginate hydrogels crosslinked by the macromolecular crosslinker alginate dialdehyde. J Mater Chem 22:9751–9758. https://doi.org/10.1039/C2JM30564J

35. Detsch R, Sarker B, Grigore A et al (2013) Alginate and gelatine blending for bone cell printing and biofabrication. Proc IASTED Int Conf Biomed Eng BioMed 2013:451–455. https://doi.org/10.2316/P.2013.791-177

36. Tuin SA, Pourdeyhimi B, Loboa EG (2016) Creating tissues from textiles: scalable nonwoven manufacturing techniques for fabrication of tissue engineering scaffolds. Biomed Mater 11(1):015017. https://doi.org/10.1088/1748-6041/11/1/015017

37. Zahedi P, Rezaeian I, Ranaei-Siadat SO et al (2010) A review on wound dressings with an emphasis on electrospun nanofibrous polymeric bandages. Polym Adv Technol 21:77–95. https://doi.org/10.1002/pat.1625

38. Zhao X, Sun X, Yildirimer L et al (2017) Cell infiltrative hydrogel fibrous scaffolds for accelerated wound healing. Acta Biomater 49:66–77. https://doi.org/10.1016/j.actbio.2016.11.017

39. Sun X, Lang Q, Zhang H et al (2017) Electrospun photocrosslink-able hydrogel fibrous scaffolds for rapid in vivo vascularized skin flap regeneration. Adv Funct Mater 27:1604617. https://doi.org/10.1002/adfm.201604617

40. Chong EJ, Phan TT, Lim IJ et al (2007) Evaluation of electrospun PCL/gelatin nanofibrous scaffold for wound healing and layered dermal reconstitution. Acta Biomater 3(3):321–330. https://doi.org/10.1016/j.actbio.2007.01.002

41. Chen W, Xu Y, Liu Y et al (2019) Three-dimensional printed electrospun fiber-based scaffold for cartilage regeneration. Mater Des 179:107886. https://doi.org/10.1016/j.matdes.2019.107886

42. Keirouz A, Chung M, Kwon J et al (2020) 2D and 3D electrospinning technologies for the fabrication of nanofibrous scaffolds for skin tissue engineering: a review. Wiley Interdiscip Rev Nanomed Nanobiotechnol 12:1–32. https://doi.org/10.1002/wnan.1626

43. Brien FJO (2011) Biomaterials & scaffolds for tissue engineering. Mater Today 14:88–95. https://doi.org/10.1016/S1369-7021(11)70058-X

44. Aderibigbe BA, Buyana B (2018) Alginate in wound dressings. Pharmaceutics 10(2):42. https://doi.org/10.3390/pharmaceutics10020042

45. Harunaga JS, Yamada KM (2011) Cell-matrix adhesions in 3D. Matrix Biol 30:363–368. https://doi.org/10.1016/j.matbio.2011.06.001

46. Del Rio A, Perez-Jimenez R, Liu R et al (2009) Stretching single talin rod molecules activates vinculin binding. Science 323(5914):638–641. https://doi.org/10.1126/science.1162912

47. Golji J, Mofrad MRK (2013) The interaction of vinculin with actin. PLoS Comput Biol. https://doi.org/10.1371/journal.pcbi.1002995

48. Bacakova M, Pajorova J, Broz A et al (2019) A two-layer skin construct consisting of a collagen hydrogel reinforced by a fibrin-coated polylactide nanofibrous membrane. Int J Nanomed 14:5033–5050. https://doi.org/10.2147/IJN.S200782

49. Ho J, Walsh C, Yue D et al (2017) Current advancements and strategies in tissue engineering for wound healing: a comprehensive review. Adv Wound Care 6:191–209. https://doi.org/10.1089/wound.2016.0723

50. Heher P, Mühleder S, Mittermayr R et al (2018) Fibrin-based delivery strategies for acute and chronic wound healing. Adv Drug Deliv Rev 129:134–147. https://doi.org/10.1016/j.addr.2017.12.007

51. Rho KS, Jeong L, Lee G et al (2006) Electrospinning of collagen nanofibers: effects on the behavior of normal human keratinocytes and early-stage wound healing. Biomaterials 27:1452–1461. https://doi.org/10.1016/j.biomaterials.2005.08.004

52. Raf C (2006) Fibrin and wound healing. Ann N Y Acad Sci 936:355–367. https://doi.org/10.1111/j.1749-6632.2001.tb03522.x

53. Laurens N, Koolwijk P, de Maat MP (2006) Fibrin structure and wound healing. J Thromb Haemost 4:932–939. https://doi.org/10.1111/j.1538-7836.2006.01861.x

54. Metcalfe AD, Ferguson MWJ (2007) Tissue engineering of replacement skin: the crossroads of biomaterials, wound healing, embryonic development, stem cells and regeneration. J R Soc Interf 4(14):413–437. https://doi.org/10.1098/rsif.2006.0179

55. Gao Y, Jin X (2019) Needle-punched three-dimensional nonwoven wound dressings with density gradient from biocompatible calcium alginate fiber. Text Res J 89:2776–2788. https://doi.org/10.1177/0040517518801198

56. Augst AD, Kong HJ, Mooney DJ (2006) Alginate hydrogels as biomaterials. Macromol Biosci 6:623–633. https://doi.org/10.1002/mabi.200600069

57. Tottoli EM, Dorati R, Genta I et al (2020) Skin wound healing process and new emerging technologies for skin wound care and regeneration. Pharmaceutics 12:1–30. https://doi.org/10.3390/pharmaceutics12080735

58. Lansdown ABG (2002) Calcium: a potential central regulator in wound healing in the skin. Wound Repair Regen 10:271–285. https://doi.org/10.1046/j.1524-475X.2002.10502.x

59. Gao Y, Jin X (2018) Characterizing the degradation behavior of calcium alginate fibers wound dressings fabricated by needle-punching process. J Appl Polym Sci 135:46670. https://doi.org/10.1002/app.46670

60. Lee W, Debasitis JC, Lee VK et al (2009) Multi-layered culture of human skin fibroblasts and keratinocytes through three-dimensional freeform fabrication. Biomaterials 30:1587–1595. https://doi.org/10.1016/j.biomaterials.2008.12.009

61. Daikuara LY, Yue Z, Skropeta D et al (2021) In vitro characterisation of 3D printed platelet lysate-based bioink for potential application in skin tissue engineering. Acta Biomater 123:286–297. https://doi.org/10.1016/j.actbio.2021.01.021

62. Albanna M, Binder KW, Murphy SV et al (2019) In situ bioprinting of autologous skin cells accelerates wound healing of extensive excisional full-thickness wounds. Sci Rep 9:1–15. https://doi.org/10.1038/s41598-018-38366-w

63. Jorgensen AM, Varkey M, Gorkun A et al (2020) Bioprinted skin recapitulates normal collagen remodeling in full-thickness wounds. Tissue Eng Part A 26(9–10):512–526. https://doi.org/10.1089/ten.tea.2019.0319

64. Kobayashi J, Kikuchi A, Aoyagi T et al (2019) Cell sheet tissue engineering: cell sheet preparation, harvesting/manipulation, and transplantation. J Biomed Mater Res Part A 107:955–967. https://doi.org/10.1002/jbm.a.36627

65. Li M, Ma JU, Gao Y, Yang LE et al (2019) Cell sheet technology: a promising strategy in regenerative medicine. Cytotherapy 21:3–16. https://doi.org/10.1016/j.jcyt.2018.10.013